Nanoscale

PAPER

Oxygen-promoted catalyst sintering influences number density, alignment, and wall number of vertically aligned carbon nanotubes†

Wenbo Shi, [ID][a] Jinjing Li,[b] Erik S. Polsen,[b] C. Ryan Oliver,[c] Yikun Zhao,[d] Eric R. Meshot,[e] Michael Barclay,[f] D. Howard Fairbrother, [ID][f] A. John Hart [ID][c] and Desiree L. Plata [ID] *[a]

A lack of synthetic control and reproducibility during vertically aligned carbon nanotube (CNT) synthesis has stifled many promising applications of organic nanomaterials. Oxygen-containing species are particularly precarious in that they have both beneficial and deleterious effects and are notoriously difficult to control. Here, we demonstrated diatomic oxygen's ability, independent of water, to tune oxide-supported catalyst thin film dewetting and influence nanoscale (diameter and wall number) and macro-scale (alignment and density) properties for as-grown vertically aligned CNTs. In particular, single- or few-walled CNT forests were achieved at very low oxygen loading, with single-to-multi-walled CNT diameters ranging from 4.8 $\pm$ 1.3 nm to 6.4 $\pm$ 1.1 nm over 0–800 ppm O_2, and an expected variation in alignment, where both were related to the annealed catalyst morphology. Morphological differences were not the result of subsurface diffusion, but instead occurred *via* Ostwald ripening under several hundred ppm O_2, and this effect was mitigated by high H_2 concentrations and not due to water vapor (as confirmed in O_2-free water addition experiments), supporting the importance of O_2 specifically. Further characterization of the interface between the Fe catalyst and Al_2O_3 support revealed that either oxygen-deficit metal oxide or oxygen-adsorption on metals could be functional mechanisms for the observed catalyst nanoparticle evolution. Taken as a whole, our results suggest that the impacts of O_2 and H_2 on the catalyst evolution have been underappreciated and underleveraged in CNT synthesis, and these could present a route toward facile manipulation of CNT forest morphology through control of the reactive gaseous atmosphere alone.

[a]*Department of Chemical and Environmental Engineering, Yale University, New Haven, CT, USA. E-mail: desiree.plata@yale.edu*
[b]*Department of Mechanical Engineering, University of Michigan, Ann Arbor, MI, USA*
[c]*Department of Mechanical Engineering and Laboratory for Manufacturing and Productivity, Massachusetts Institute of Technology, Cambridge, MA, USA*
[d]*Department of Civil and Environmental Engineering, Duke University, Durham, NC, USA*
[e]*Physical and Life Sciences Directorate, Lawrence Livermore National Laboratory, Livermore, CA, USA*
[f]*Department of Chemistry, John Hopkins University, Baltimore, MD, USA*
†Electronic supplementary information (ESI) available. See DOI: 10.1039/c6nr09802a

Introduction

In spite of the staggering promise of carbon nanotubes (CNTs) to transform the electronics,[1–5] energy storage,[6] and water treatment sectors,[7] few CNT-enabled technologies have been translated to commercial success because of limitations in achieving simultaneously high yield and quality in bulk syn-

thesis. In particular, chirality control,[8,9] alignment and direction of growth,[5,10] and reproducibility[11,12] have been persistent challenges in chemical vapor deposition (CVD) CNT synthesis. Briefly, CVD synthesis of CNTs relies on the conversion of carbonaceous gases into a solid material with the assistance of catalytic nanoparticles (*i.e.*, *via* heterogeneous catalysis). Poor reproducibility in CNT synthesis *via* CVD has been attributed to fluctuations in ambient and reactor-sorbed water vapor,[11] as well as to carbonaceous deposits inside reactors leading to growth hysteresis.[13] The mechanisms of these impacts are thought to derive from (a) the influence of water or oxygen on the growth gases (*i.e.*, carbon-containing gases) and/or (b) the formation or removal of carbonaceous deposits on the catalyst nanoparticles (*i.e.*, removal *via* etching with water vapor). Indeed, several oxygen-containing gases (*e.g.*, H_2O,[14] O_2,[15] and CO_2 [16]) have been shown to enhance CNT formation to an extent (see summary in Table S1†), where excess levels of oxygen-containing compounds can result in etching of the CNTs themselves.[17–21] Specifically, oxygen-containing species

are reported to improve the CNT quality, to enhance catalyst activity and prolong catalyst lifetime, thus increasing CNT yield in bulk synthesis.[14,17,22] In addition, type-selected CNTs (e.g., SWCNT forests,[14] semiconducting-enriched SWCNTs,[23,24] metallic-abundant SWCNTs[25]) were also achieved via water addition. The benefits of oxygen-assisted methodologies are promising for mass production of high-quality CNTs, but add one more operational parameter that impacts manufacturing reproducibility and lacks in-depth understanding and a priori rationale for control.

To date, all of the proposed mechanisms by which oxygen-containing materials influence CNT growth have been related to gas-phase processes or reactions between the oxidant and reduced carbon phases. In contrast, little attention has been devoted to the effects of the reactive atmosphere on the metal catalyst itself. Studies in other heterogeneous catalysis systems, such as CO oxidation, have demonstrated that oxygen-containing species affect the catalyst size and shape.[26,27] Further, differences in catalyst particle morphology can influence the activity and product selectivity, especially for those at the nanoscale.[28–30] For catalytic CNT growth, the question remains as to how oxygen and water vapor affect catalyst nanoparticle evolution, both prior to and during CNT synthesis.

The environmental effects (i.e., those derived from the gaseous atmosphere of intentional or unintentional additives such as air, CO, O_2, H_2, H_2O, NO, and N_2) on a wide range of catalytic models have been previously investigated in an effort to enhance their performance.[26] For example, Pt/oxides or amorphous carbon,[31–41] Pd/oxides,[42–44] Au/oxides or amorphous carbon,[45,46] Cu/oxides,[47,48] and Co/oxides[49] were studied in the context of one or more of the following reactions: exhaust gas catalytic conversion, CO oxidation, methanol synthesis, and Fischer–Tropsch synthesis. Perhaps the most well studied catalytic system of all time, the Pt/Al_2O_3 in the automobile catalytic converter, is known to undergo sintering in response to oxidizing gaseous atmospheres.[31,38] In contrast, oxygen can be used for Pt nanoparticle redispersion,[50] which is enabled presumably by volatile PtO_x species detaching from the large nanoparticle clusters and subsequently decreasing the metallic Pt nanoparticle size.[51] While it is held that oxygen induces sintering in the majority of catalyst systems, these counterexamples suggest that a more detailed understanding of the environmental effects on catalyst nanoparticle morphology could be a means of suppressing sintering and controlling the catalyst shape during reaction conditions.

Unlike the extensive studies of Pt or Pd-based catalytic systems, the effects of gaseous environments on Fe-based catalysts are rarely studied, despite their broad significance in mediating water–gas shift reaction,[52] Fischer–Tropsch synthesis,[53] oxygen reduction,[54] the recently discovered non-oxidative conversion of methane,[55] and being the foremost employed catalysts for carbon nanotube growth.[56,57] The atmospheric-pressure CVD reactors commonly used for CNT formation often contain some levels of residual H_2O and O_2, even in the absence of intentional addition of those gases.[11] Unintended operational nuances (e.g., purging time variations after sample exchange, the lack of a seal or baking procedure during down time, changes in relative humidity leading to differences in adsorbed water levels, gas-permeable tubing, and a lack of sensors to indicate the internal moisture) can give rise to variation in internal levels of H_2O and O_2, leading to non-repeatable results and biased data interpretation. While the impact of these gas species is evident, conflicting results have been observed (i.e., H_2O can suppress ripening,[58,59] or not[20]). These apparent disparities could result from the difficulty associated with controlling moisture and oxygen levels in CVD systems, and a rationally-designed reactor must be used to eliminate hysteresis and batch-to-batch heterogeneity. Understanding these trace-gas effects is critical to eliminate operational nuances and to design effective synthesis equipment, whose complexity is a critical cost driver for industrialization of CNTs and their suitability for specific applications.

For the ultimate practical applications of vertically aligned CNTs (VA-CNTs) forest, tunable CNT diameter, number of walls, alignment, and density are crucial for exhibiting their envisioned outstanding mechanical, thermal, and electrical properties.[60,61] Considering the strong correlation between CNT structural properties and catalyst morphology,[62] identifying the roles of the gaseous oxidants in the catalyst formation process for CNT growth could enable reproducible CNT manufacturing with controllable properties. Here, we address this issue systematically and deconvolute the roles of O_2, H_2, and H_2O in catalyst evolution from experimental results. In this study, VA-CNTs were grown on catalyst-coated silicon substrates by atmospheric-pressure CVD in a specialty tube furnace.[11,12] Under variable atmospheres of inert gas (He or Ar), H_2, and O_2, catalyst nanoparticles were generated by annealing a 1 nm Fe film on a 10 nm Al_2O_3 support on a silicon substrate. VA-CNTs were then grown using C_2H_4 as the carbon source with a "fast heat" technique.[11,21] A hygrometer downstream of the tube furnace was used to measure the moisture content in the effluent, and experiments were initiated only after a stable water content was achieved.

Experimental

CNT synthesis

Vertically aligned carbon nanotubes (VA-CNTs) were grown by catalytic chemical vapor deposition in a 1″ Lindberg Blue M tube furnace outfitted with a downstream Dewpoint hygrometer (Kahn Cermet II) to monitor moisture in the reactor. Substrate-affixed catalysts were prepared by electron beam deposition of 1 nm Fe over 10 nm Al_2O_3 on prime n-type Si (100) wafers.[63] Note that the Fe was deposited as zero-valent Fe but is easily oxidized by ambient oxygen levels prior to loading into the reactive chamber, and this Fe oxide must be reduced (i.e., via annealing described below) prior to successful catalyst dewetting, CNT nucleation, and elongation

(Fig. S1†).[62,64,65] Also note that alumina was directly evaporated from 99.99%-purity Al_2O_3 crystals at high vacuum, thus, the stoichiometry should be conserved. Gases were delivered to the reactor in three phases: (1) flushing with 1000 sccm ultra high purity (UHP) He for 10 min at room temperature and then heating to 775 °C, and after dewpoint stabilization, the substrate and quartz tube were rapidly shifted into the heated zone (*i.e.*, in a "fast heating" approach), (2) annealing for 10 min under 400 sccm UHP H_2 plus variable amounts of UHP He (20 sccm or greater) and 0.5% O_2 in He (80 sccm or less) in order to reach a total of 100 sccm (*i.e.*, 500 sccm for all gases during annealing); and finally, (3) growing under 100 sccm H_2, 100 sccm C_2H_4, identical amount of 0.5% O_2 in He as selected for the annealing process and variable amounts of UHP He to make up 500 sccm total flow for 15 min. For all experiments, we minimized adsorbed water vapor by flushing the reactor overnight with 1000 sccm UHP He. The 0–800 ppm O_2 concentration range was chosen as a constrained window of a previous study.[11]

To test the effect of oxygen on catalyst annealing at distinct hydrogen levels, we varied the H_2 flow rate from 100 sccm to 400 sccm, 0.5% O_2 in Ar from 0 to 10 sccm and kept the total flow rate constant (500 sccm) using a balance of UHP Ar. This set of data is presented in Fig. 3 and 4.

In order to test the effect of water and oxygen independently, one other series of experiments was conducted using a specialty-designed atmospheric-pressure furnace,[12,66] which can load new catalysts without exposing the tube to the ambient atmosphere, thereby minimizing adsorbed water vapor and reducing the time necessary to return to dry reactor conditions.

Critically, we underscore that the O_2 added was small compared to the content of H_2 in the gas environment (*i.e.*, less than 1 : 1000 for O_2 : H_2). Moreover, the reaction between O_2 and H_2 is highly favored thermodynamically,[21] and residual O_2 contents will be lower than input recipe levels. As a result, we operate under the assumption the Fe catalyst is reduced to zero-valent Fe during the annealing step (*i.e.*, consistent with Hofmann *et al.*'s[64] findings and in light of the high H_2 : O_2 ratios). Indeed, Plata *et al.*'s[67] CNT growth mechanism invoked the presence of reduced Fe for CNT formation. Nevertheless, Teblum *et al.*[68] demonstrated that it is possible to form CNTs from oxidized Fe_xO_y species, albeit with less efficiency than metallic Fe.

Material characterization

The catalyst morphology was interrogated by scanning electron microscope (SEM; Hitachi SU-70 SEM at 15 kV) and atomic force microscope (AFM; Veeco Dimension Icon; tapping mode). The electronic structure and elemental distribution over and within the catalyst support were studied using X-ray photoelectron spectroscopy (XPS; PHI 5600 at P_{base} less than 5×10^{-9} Torr with Mg Kα radiation (1253.6 eV, 15 kV, 300 W)), XPS with Ar ion beam etching to enable depth profiling, and X-ray diffraction and X-ray reflectivity (XRD and XRR, respectively, both using a Rigaku SmartLab X-ray diffractometer (Cu Kα radiation operating at 45 kV and 200 mA)). XPS spectra

were analyzed by CasaXPS®, and the concentrations of Fe, Al, and Si were determined from each sample by fitting the Fe (2p), Al (2p) and Si (2p) regions after assigning Shirley, Linear, and Linear background, respectively. Cross-sectional transition electron microscopy (TEM) samples were prepared by FEI Helios NanoLab 660 SEM focused ion beam (FIB) at CUNY Advanced Science Research Center Facility in New York, NY and imaged by FEI Tecnai Osiris at 200 kV.

CNT alignment was characterized using SEM (Hitachi S-4700 Cold Cathode Field Emission at 5 kV) and image analysis to calculate the Herman's Orientation Factor (HOF) following Xu *et al.*[69] CNT outer diameter and wall number were analyzed by FEI Tecnai G^2 Twin TEM at 200 kV (80 counts per sample) and FEI Tecnai Osiris TEM at 200 kV, respectively. Raman spectra were collected on a Hobriba Jobin Yvon LabRam Aramis Microscope with a 633 nm excitation laser (HeNe).

Results and discussion

Key findings

Molecular oxygen, rather than water, was found to tune CNT alignment, density, diameter, and even wall number, enabling the selection of single- and few-walled VA-CNTs. This controllability was associated with the underlying O_2-mediated impacts on catalyst sintering, where higher O_2 environments promoted sintering and lower O_2 atmospheres prevented the growth of large catalyst particles, and these effects could be mitigated by the relative H_2 loading. Further investigation revealed that the enhanced mobility of Fe-on-Al_2O_3 in O_2-rich conditions proceeded by surface migration, where no evidence of subsurface diffusion was observed. The mechanisms of catalyst surface atom migration *versus* subsurface diffusion are not only transformative for their implications for CNT synthesis, but are potentially universal for the sintering of all oxide-supported metal catalysts.

Effect of oxygen on CNT alignment and catalyst morphology

First, CNT forests were synthesized under identical conditions but with different amounts of added O_2. CNT alignment generally decreased, where the Herman's Orientation Factor (HOF; an order parameter that goes from 0 to 1 for random to perfect alignment, respectively)[69,70] varied from 0.73 to 0.51 as O_2 partial pressure increased (over 0 to 800 ppm O_2, respectively), exhibiting a maximum alignment at 300 ppm O_2 (0.87 HOF) (Fig. 1a; SEM images are shown). Consistent with previous understanding that CNT catalyst particle density (and subsequent nucleation) enhances the alignment of CNTs through enhanced inter-tube mechanical coupling,[71,72] there was a distinct and monotonic decrease in the number density of catalyst nanoparticles (Fig. 1b; 2056 to 456 μm^{-2}, AFM images are shown) and increase in catalyst particle diameters and heights (Fig. 1c and S2;† 12 ± 3 nm to 17 ± 3 nm diameter; 8 ± 1 to 15 ± 2 nm tall over 0–800 ppm O_2, respectively; AFM and SEM images are shown), which corresponded with the decrease in
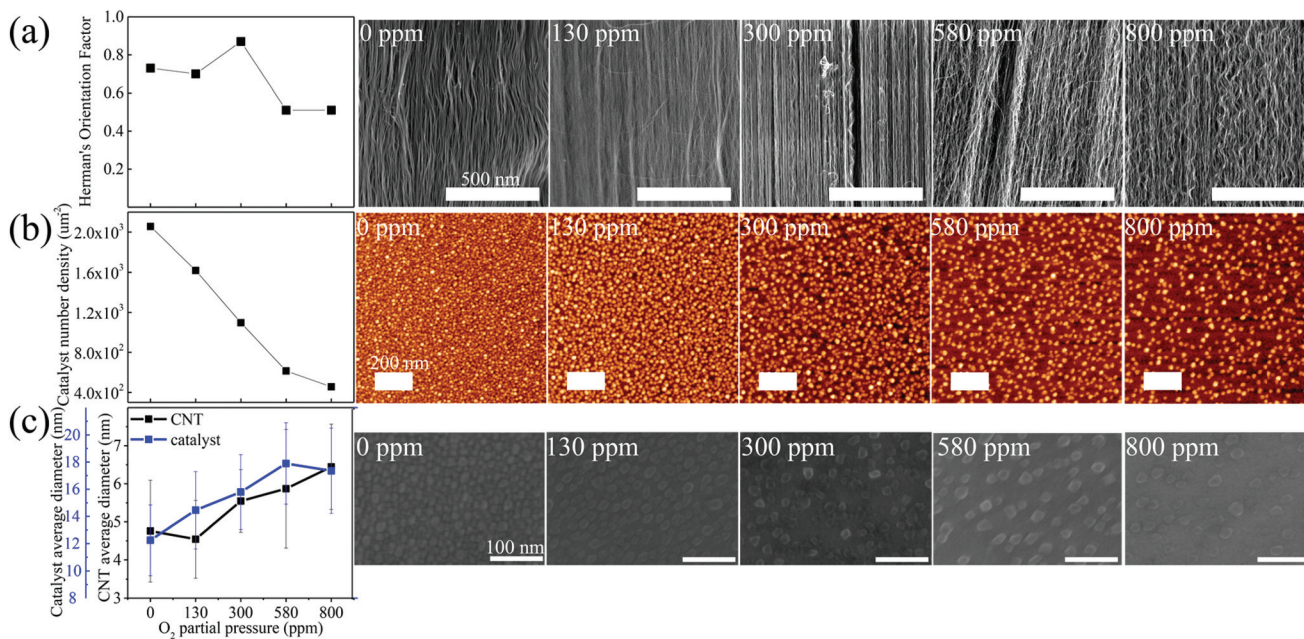
Fig. 1 Effects of O_2 on annealed catalysts and resultant CNT properties. In all experiments, 0.5% O_2 balanced by He was delivered to make up the O_2 partial pressure from 0 to 800 ppm. (a) The alignment (Herman's Orientation Factor; where 1 is perfect alignment) and corresponding SEM images, (b) catalyst nanoparticle number density and corresponding AFM images, and (c) diameter of CNTs, and diameter of catalyst nanoparticles and corresponding SEM images, changed with O_2 partial pressure. Error bars (standard deviation) in (c) were calculated from $n = 80$ for CNT diameter and from at least $n = 53$ for catalyst diameter.

CNT alignment. Here, we note that we did not measure catalyst nucleation efficiency[62] (possible *via* X-ray scattering techniques[65]), but acknowledge its importance for CNT density and alignment. For example, it is possible that higher residual O_2 contents could give rise to partially-oxidized Fe catalyst islands, and this could result in decreased CNT nucleation efficiency (due to their reported decreased catalytic activity by Teblum *et al.*[68] or completely losing graphitization ability by Hofman *et al.*[64]) and reduced alignment. While the decreased catalyst density (Fig. 1b) is sufficient to explain the reduced alignment, one cannot rule out the possibility of partial Fe oxidation and reduced CNT nucleation efficiency as a contributing factor to reduced CNT alignment at high levels of O_2. *Ex situ* X-ray photoelectron spectroscopy (XPS) analysis was not useful to make this determination, since atmospheric O_2 level (approximately 20.95%) readily oxidizes Fe: the *ex situ* XPS spectrum of Fe (2p) (Fig. S3†) presented chemically identical Fe nanoparticles across a range of oxygen loadings (*i.e.*, oxidized to FeOx after being exposed to air). This reduces (but cannot rule out) concerns that catalyst size differences shown in SEM and AFM images (Fig. 1) were simply due to variation in oxidation state (*i.e.*, FeOx is larger than Fe). Nevertheless, the concomitant increase in particle size and decrease in particle number density support the growth of larger particles, rather than a change in oxidation state. While no direct measurement of catalyst oxidation state was possible during the reaction, O_2 residuals were very small in the reactor compared to bulk H_2 in all of the experiments, and we do not expect significant Fe catalyst oxidation *in situ*. Finally, there

was no evidence of catalyst die off or weakening at trace O_2 loadings due to severe catalyst oxidation (Fig. S4†). While the general trends between particle number density and tube alignment were consistent with theory, the catalyst particle dynamics could not explain the enhanced alignment at 300 ppm O_2. Note that besides the number density, functional groups (extending along radial direction outside tubes) derived from the incorporation of different alkynes (appearing in the gas composition) into CNT structure might impact the interaction forces between neighbouring tubes, thus influencing CNT alignment. Investigating the possibility that gas-phase composition (rather than catalyst morphology) influenced tube alignment, we observed a local maximum in methyl acetylene (*i.e.*, propyne) abundance under the 300 ppm O_2 condition (Fig. S5†). While rigorous demonstration of a causative relationship between gas chemistry and tube alignment is pending work from the Plata lab, methyl acetylene is a known VA-CNT growth enhancer that could potentially exert influences on CNT alignment[67,73,74] beyond the dominant influence of the catalyst packing density.[69]

Previous reports of the benefits of O in VA-CNT synthesis derive from balancing C and H radicals,[15] selectively synthesizing SWCNT,[75] and etching amorphous carbon to maintain catalyst activity,[76] as well as the detrimental effects associated with changing Fe oxidation state and thus reducing catalyst activity,[68] and, finally, etching CNTs when O_2 was extremely intense.[21] In addition to these effects, our results indicate that O_2 also plays an important role *via* the catalyst geometry, giving rise to variations in CNT diameter and overarching

forest morphology. In particular, larger CNT diameters were found in the presence of abundant oxygen (4.8 ± 1.3 to 6.4 ± 1.1 nm over 0–800 ppm O_2; Fig. 1c). The relative increase of the catalyst particle diameter (approximately 40%; confirmed by SEM) is close to the relative increase in CNT diameter (approximately 30%; confirmed by TEM), and this is consistent with previous demonstrations of the strong dependence of CNT diameter on catalyst diameter.[77,78] Note that the size of the catalyst particles were larger than the CNTs themselves (Fig. 1c and S2†), suggesting a "perpendicular mode" nucleation (i.e., CNTs attaching on top of the catalyst dome rather than around its widest circumference).[79,80] Due to this attachment geometry, low diameter MWCNTs gave way to few-walled CNTs at the lowest O_2 loadings (Fig. 2 and diameter distribution available in Fig. S6a†), as revealed by the emergence of a radial breathing mode (RBM, full Raman spectra are avail-

able in Fig. S7†) and confirmed by high-resolution TEM images (wall number distribution available in Fig. S6b†). This is significant: few- and single-walled CNTs often rely on the use of unique catalysts (e.g., Co/Mo[81–83] or Ni/Y[84] mixtures) or unique catalyst deposition techniques (e.g., other than the readily-scalable metal thin films). Here, we have demonstrated that simply exerting control over the oxygen content of the reactive atmosphere can provide a route toward single and few-walled vertically aligned CNTs using earth-abundant,[85] e-beam deposited Fe thin films. Manufacturers could potentially offer a range of products of variable tube diameter and wall numbers through simple manipulation of the reactive atmosphere; i.e., by exerting gas-phase controlled catalyst morphological changes.

Oxygen's role mitigated by high hydrogen content: deconvoluting the effect of water vapor

Practically speaking, during 'C-free' annealing steps, O_2 residuals in most atmospheric-pressure CVD reactors will have some fraction of O_2 that remains diatomic oxygen and some fraction that is converted to water vapor (H_2O). This balance will rely on the H_2 content in the atmospheric reactor as well as the temperature. To assess the role of this trace, residual O_2 and associated (i.e., thermally generated) H_2O, we investigated the effect of sub-100 ppm O_2 levels over a range of comparatively large H_2 operating ratios seen in the literature. Oxygen's effect on the catalyst annealing process was most dramatic in low hydrogen environments (0.2–0.4 atm), but effectively eliminated in high hydrogen atmospheres (0.6–0.8 atm; Fig. 3 and S8†). High-resolution scanning electron microscopy (SEM)
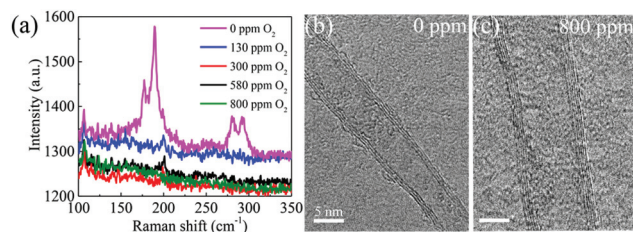

Fig. 2 Effects of O_2 on as-grown CNT wall numbers. Lowest O_2 loading was found to lead to thin CNTs with fewer walls. (a) Raman spectra indicated MWCNTs gave way to smaller diameter few-walled CNTs at the lowest O_2 loadings, and this finding was supported by high-resolution TEM images (b and c).
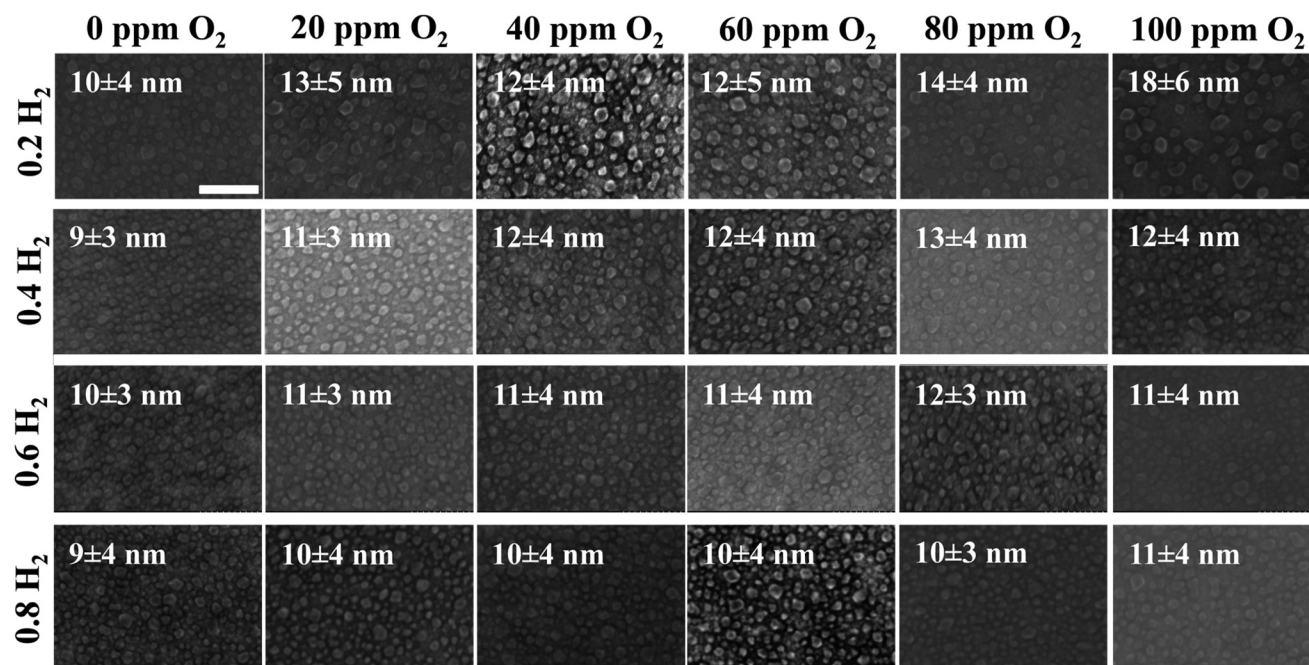

Fig. 3 The evolution of Fe-on-Al_2O_3 on a Si support following annealing at various O_2 and H_2 abundances. Annealing was conducted at 775 °C for 10 min in a total flow of 500 sccm (H_2 and O_2 balanced with Ar). SEM image analysis of at least $n = 76$ was used to calculate the total mean and standard deviation of the particle diameters. The scale bar in the upper left image is 100 nm and is consistent throughout the images.

revealed that catalyst nanoparticle diameter increased with increasing O_2 content at low H_2 (0.2 atm), but was unchanged at high H_2 (0.8 atm); *e.g.*, nanoparticle diameters ranged from 10 ± 4 to 18 ± 6 nm over 0–100 ppm O_2 at low H_2 and 9 ± 4 to 11 ± 4 nm over the same O_2 range at high H_2. Catalyst particle height measured by AFM revealed the same general trend of larger particle sizes at high O_2 loadings, albeit with some non-monotonic behavior (discussed in Potential Mechanisms; see mechanism b) at lower H_2 levels (Fig. 4a). ANOVA analysis confirmed that the particle height trends as a function of O_2 show statistically significant differences between H_2 loadings tested ($p < 0.05$) (Fig. S9†). In the absence of O_2, H_2 had no effect on the resultant catalyst size, suggesting that O_2 has a dominant influence over catalyst particle size (catalyst diameters ranged from 10 ± 4 to 9 ± 4 nm over a large range in H_2 (0.2–0.8 atm) at 0 ppm O_2). Nevertheless, H_2 is critical to the reduction and dewetting of the Fe film,[86] and our observations in a zero-H_2 condition confirm this result (Fig. S1†).
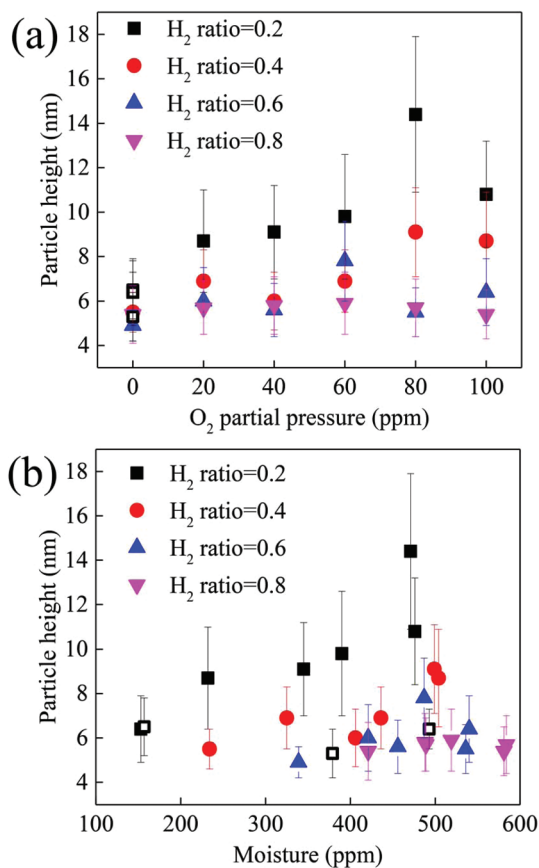

Fig. 4 Isolated effects of O_2 and H_2O's influence on catalyst dewetting. Catalyst particle height changed with (a) O_2 partial pressure and (b) moisture. Note that these are from the same experiment set, in which O_2 and water vapor co-vary. AFM image analysis was used to calculate the total mean and standard deviation of the particle heights. Open squares represent control experiments of varying moisture in an O_2-free system and 0.2 H_2 (*i.e.*, O_2 and water are not co-varied here). Error bars represent $\pm$ standard deviation calculated over at least $n = 684$ particles.

As molecular hydrogen is present in the gas atmosphere during the entire VA-CNT growth process, any test of the effect of diatomic oxygen will necessarily give rise to water vapor through a highly exothermic reaction between H_2 and O_2. To ensure that the observed catalyst morphology changes at variable O_2 were not merely the result of differences in moisture, we used a water bubbler to generate moisture levels consistent with those derived from our added O_2 experiments (150 ppm to 500 ppm H_2O at 0.2 H_2; SEM and AFM images available in Fig. S10†), but in an O_2-free system (*i.e.*, one in which no O_2 is intentionally added).[12] Catalyst films annealed at different moisture levels in the absence of O_2 exhibited particle sizes that were identical to each other (Fig. 4, open symbols) and close to our particles formed at 0 ppm O_2 in our added O_2 experiments. Thus, the observed catalyst morphology differences are due to relative H_2 and O_2 levels, rather than differences in moisture, as previously postulated.[11,58]

Beyond some basal requirement of H_2 to reduce and dewet a Fe thin film into catalyst islands (Fig. S1† and previous work),[86–88] our observation that H_2 had no effect on catalyst ripening in the absence of O_2 might be consistent with the finding of In *et al.*[89] Briefly, In *et al.* demonstrated that variation of annealing treatment *time* in H_2 didn't impact the catalyst nanoparticle ripening process in their O_2-free system. Further, Hu *et al.* proposed that the mixing between Fe and Al_2O_3 underlayers is an entropically driven thermodynamic inevitability, and H_2 functionally "reverses" this process (*i.e.* driving the Fe backward onto the surface).[90] Similarly and also consistent with our results, Sakurai *et al.* suggested that H_2 helps maintain a high Fe surface tension that inhibits Ostwald ripening (*i.e.*, impedes surface migration).[91] Our results, and others in heterogeneous catalysis,[31,92] suggest that the O_2 content of the ambient gas composition has critical implications for particle coarsening *via* Ostwald ripening.

Surface *versus* subsurface diffusion

Two important phenomena are thought to control the catalyst size and number density: Ostwald ripening and subsurface diffusion.[93] Ostwald ripening describes a process in which atoms migrate from small particles to large particles, resulting in the loss of small particles and growth of large ones and a decreased number density.[94] Subsurface diffusion is a process in which the catalytic atoms diffuse into the substrate layer, reducing the size of the nanoparticles that remain on the surface and potentially rendering the remaining particles ineffective toward nanotube deposition.[93] As a result, subsurface diffusion has been proposed as a root cause of abrupt CNT growth termination.[94] While Ostwald ripening was pronounced in our studies in O_2-rich atmospheres, it was unclear if the reduced particle density at high O_2 was partially due to subsurface diffusion (Fig. 5a–d; *t*-test between particle diameter in the absence ($n = 282$) and presence ($n = 53$) of O_2 was significantly different; 95% confidence interval).

In order to evaluate the potential of subsurface diffusion, we mapped the elemental composition of our multilayer cata-
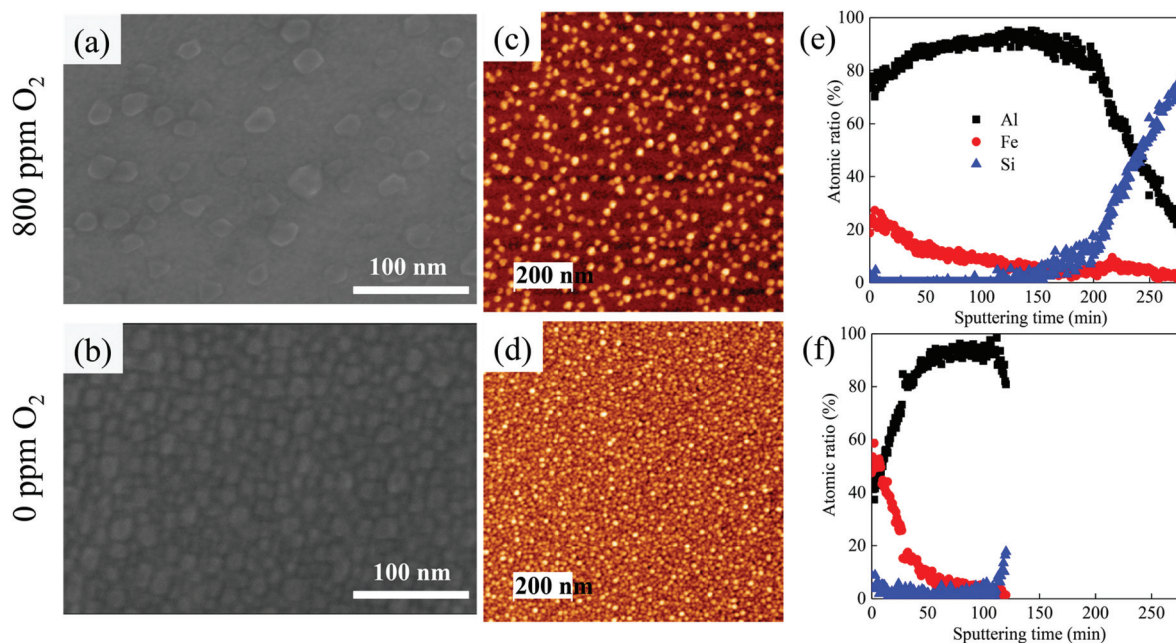
Fig. 5 Ostwald ripening of Fe thin films on alumina underlayers (1 nm Fe on 10 nm Al_2O_3 on a Si support) is influenced by oxygen content. Following annealing at 775 °C for 10 min under 400 sccm H_2 and 100 sccm He with or without O_2, SEM images (a, b); AFM images (c, d); and XPS depth profiling of the Fe/Al/Si ratio in the substrate (e, f) in the presence (800 ppm) and absence (0 ppm) of O_2, respectively. We caution that surface morphology influences the distribution of elements in the apparent depth of XPS depth profile (i.e., higher alumina content can be interpreted as more exposed alumina between Fe catalyst islands or subsurface mixing of Fe into the alumina), thus 'sputtering time' is utilized in (e, f) as the abscissa to present the XPS data instead of commonly seen 'depth', which would only be valid for smooth surface. Note here that sputtering was conducted until there was a sharp increase in the silicon signal and that sputtering time is not linearly correlated with depth.

lyst thin films by XPS depth profiling (Fig. 5e and f) and cross-sectional TEM (Fig. 6). The XPS depth profiling in the cases of high and no O_2 revealed unique patterns. First, in the absence of additional O_2, the surface Fe and alumina contents were approximately 60 and 40%, respectively. However, in the 800 ppm O_2 case, the surface alumina content was much higher (approximately 80%), with a correspondingly lower Fe content (approximately 20%). Second, in both cases the Fe content exhibited an exponential decrease with increasing sputtering time, but at high O_2 this decay occurred over a longer etching time (related to spatial depth into the film). These differences could be explained by either (1) diffusion of Fe into the Al_2O_3 underlayer at high O_2 or (2) variations in catalyst topography. Historically, element depth profile analysis (e.g., XPS and secondary ion mass spectroscopy (SIMS)) has been used to demonstrate the degree of subsurface diffusion of Fe-on-Al_2O_3 systems.[90,93,95–97] However, because the ion ablation pattern (i.e., a raster pattern) scans the surface without bias, one can imagine that a proportionately larger (with respect to height and diameter) Fe catalyst island with more exposed alumina surrounding it would give rise to an XPS depth profile that displayed both (a) an elevated signal of alumina and proportionately depleted Fe near the surface and (b) a prolonged Fe die-off (i.e., an apparently "deeper" Fe signal). In other words, a raised-topography would present similarly to subsurface diffusion, even though no such subsurface Fe migration existed. Therefore, XPS on its own was not
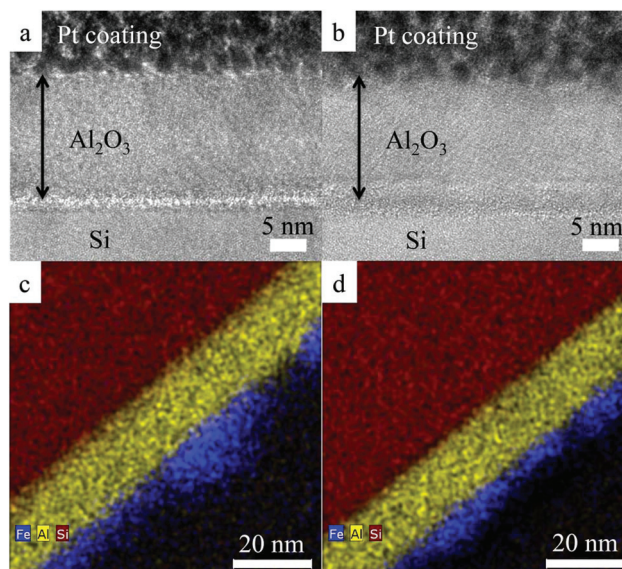

Fig. 6 Cross-sectional TEM images (a, b) and energy-dispersive X-ray spectroscopy (EDX) elemental maps (c, d) in scanning transmission electron microscopes (STEM) images of the catalyst annealed at two different gas environments. (a, c) was annealed at 0.2 H_2 and 100 ppm O_2. (b, d) was annealed at 0.8 H_2 and absence of O_2. Note that these environments were chosen as representative extreme cases in the matrix represented in Fig. 3.

conclusive, and further investigation was needed to evaluate subsurface diffusion in our experiments.

To test for subsurface diffusion in an O_2-abundant environment, we compared the cross-sectional TEM images of the two extreme conditions of the annealing matrix (*i.e.*, 100 ppm O_2 at 0.2 H_2 and 0 ppm O_2 at 0.8 H_2; out of all the possible choices shown in Fig. 3). In the TEM images (Fig. 6a and b), most of Fe atoms were buried inside the Pt coating layer (coated for SEM/Focused Ion Beam (FIB) for cross-sectional TEM sample preparation) and no obvious Fe was observed in the Al_2O_3 layer in either sample, while previously reported subsurface diffusion presented apparent dark dots (*i.e.*, Fe) inside the Al_2O_3 layer in the cross-sectional TEM images.[94,95] The thickness of Al_2O_3 was around 16 nm (higher than the nominal 10 nm) and consistent with the X-ray reflectivity (XRR) fitting results (Fig. S11†). Elemental mapping (Fig. 6c and d) revealed that, in both samples, Fe was sitting on the surface of the Al, indicating few Fe atoms diffused into the layer of Al_2O_3 whether O_2 was present or not (element depth profile available in Fig. S12†). Thus, O_2 promoted only surface diffusion (*i.e.*, Ostwald ripening) and not subsurface diffusion. The Fe mapping shapes of these two samples were consistent with the particle size and the distance between neighboring particles as shown in SEM images (Fig. 3) and confirmed the interpretation of the XPS depth profile (Fig. 5e and f) as reflective of surface morphology effects rather than subsurface diffusion.

While Ostwald ripening has negative influences on CNT growth such as density decay, unfavorable alignment, and eventual growth termination, it is one of the dominant mechanisms for the transformation of an e-beam-deposited Fe thin film to suitable size nanoparticles (*i.e.*, islands or clusters) for CNT growth. Thus, modulating and leveraging this process is critical for consistent and repeatable vertically aligned CNT growth, and this can be done through precise control of the gas environment. Oxidizing environments are generally recognized as favorable for the catalyst sintering process,[26] and recent *in situ* studies have observed oxygen-induced sintering in metal nanoparticle-oxide support systems.[31,32,39,41,44,92] In contrast, water has been proposed to stabilize small Fe nanoparticles by bonding oxygen or hydroxyl species on the surface to reduce Fe atom migration rate across the substrate surface.[58] Compared with our study, the 0.5 nm Fe thickness used by Amama *et al.*[58] (*versus* 1 nm in this study) could lead to heterogeneity in the initially dewetted nanoparticle size distribution due to discontinuous deposition[98,99] or large interparticle distances due to the lower mass loading. As a result, large Fe migration distances may have manifested as local stability against Ostwald ripening[36,100] in the earlier work by Amama *et al.* Furthermore, supplying moisture with a large carrier flow rate (200 sccm) but without a hygrometer to indicate humidity level could ultimately give rise to confounding results. Here, we observed severe ripening in high O_2 environments, and no influence of water vapor in the absence of O_2 (this work and Li *et al.*[12]), which is consistent with generally held nanoparticle formation trends in oxidizing environ-

ments and could be explained *via* the mechanisms described below.
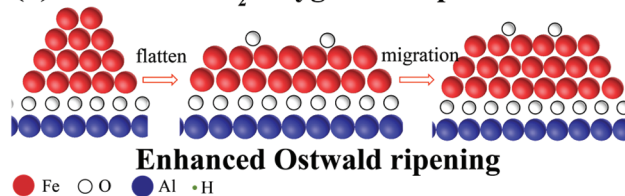
Potential mechanisms of oxygen-enhanced Ostwald ripening

A reactive atmosphere could influence the catalyst evolution process in at least three ways: affecting the strength of the Fe metal–metal bonds; affecting the binding energy between the Fe metal particles and the Al_2O_3 substrate; or altering the physicochemical character of the Al_2O_3 substrate itself. We have already ruled out the generation of H_2O as a factor and here propose two mechanisms that draw on the impact of O_2 on these three processes: (a, Scheme 1a) oxygen-deficits could evolve in the Al_2O_3 layer, leaving local positive charges that impede the surface and subsurface migration of Fe atoms (under low O_2 atmospheres) or (b, Scheme 1b) oxygen adsorption could enable wetting or atom migration and particle growth (under high O_2 atmospheres). Considering the oxygen deficit mechanism (Scheme 1a), we note that the electrostatic force between a partially positive substrate and a positively charged Fe atom[64] would prevent diffusion on the surface and immobilize the small Fe nanoparticles. Thus, in this low-O_2 situation, the ripening effects are not pronounced. When O_2 is abundant, it could replace oxygen defects in the Al_2O_3 structure, and the Fe atom would have higher mobility over the surface, as observed. The status of the substrate in the oxide-supported metal catalyst plays an important role in catalyst evolution and CNT growth.[95,101] In our study, evidence for existence of the oxygen deficiencies in the Al_2O_3 underlayer include: (a) a general increase in Al_2O_3 mass density with increasing O_2 partial pressure (Fig. S11†), where higher density corresponds to lower oxygen deficiency, lower charging, and less impediment to Fe migration. Amama *et al.*[95] confirmed that the observed Fe morphology and wettability of Fe is associated with the density of substrate (*i.e.*, the more sub-
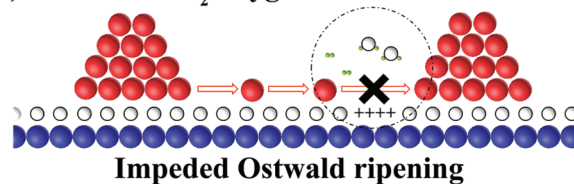
Scheme 1 Potential mechanisms of (a) impeded Ostwald ripening in low O_2 environments and (b) enhanced Ostwald ripening in high O_2 environments. In the former (a), oxygen vacancy and surface charging formation in Al_2O_3 substrate prevent migration of Fe atoms in a reducing environment. In the latter (b), oxygen adsorption in Fe particles causes wetting by several potential mechanisms described in the text.

strate density, the more mobility). (b) The Al_2O_3 is confirmed to be amorphous after annealing (Fig. S13†), and the fact that the Al (2p) binding energy upshift to higher energies under O_2 might indicate that AlOx was approaching stoichiometric O loading (Fig. S14†).[102] Note that aluminum itself can occupy only the 0 and +III oxidation states, and the phenomenon of oxygen deficiency manifests itself through the non-stoichiometric solid. A related phenomenon of oxidation state switching has been previously reported in zirconia systems,[103] but remains contentious. Last, there is concern that such subtle shifts in binding energy could be the result of instrumental tuning, variance, or interpretation errors. Nevertheless, a measurable change in the alumina density corresponded with a measurable change in the overlying Fe nanoparticle size and morphology, and chemically-induced changes in the under-layer could plausibly give rise to changes in the Fe atom surface migration.

The oxygen adsorption mechanism (Scheme 1b) has more support in the extant literature. For example, oxygen adsorption in the supported catalyst is generally reported to lower the surface tension of the catalytically active metal particles.[104,105] In this theory, the driving force for the metal catalyst dewetting (*i.e.*, formation of nanoparticles from a thin film) is the difference in surface energy of the catalytic metal, Fe, and of the support layer, Al_2O_3 (*e.g.*, 2.12–2.22 J m^{-2} and 0–0.1 J m^{-2}, respectively).[106,107] In O_2-free systems, the Fe nanoparticles remain in a high-surface-tension status and maintain small diameters. In abundant O_2 environments, oxygen adsorption lowers the surface tension of the nanoparticles and causes wetting (*i.e.*, catalyst nanoparticle spreading[108,109]), which leads to larger diameter particles. For example, at 0.2 H_2, there is a sudden drop in particle height when O_2 partial pressure increased from 80 ppm to 100 ppm, while particle diameter kept increasing, which indicates the formation of flatter nanoparticles (Fig. 3 and 4). Additional postulated mechanisms for the observed impact of oxygen on particle sintering include: oxygen's ability to weaken the metal–metal bond,[110] form volatile oxygen–metal complexes,[111] and strengthen metal–oxide support interaction (*i.e.*, leading to a more energetically favored metal–metal bond breaking from parent nanoparticles),[36] thus enhancing the possibility of metal atom detachment[100] and promoting Ostwald ripening.

In addition to the aforementioned mechanisms, surface hydroxyl is commonly observed on oxide surfaces,[112] and thought to have the potential to influence metal atom mobility on oxide surface.[58] Here, if surface hydroxide were playing a role as Amama *et al.*[58] proposed (*i.e.*, inhibiting metal Fe migration), we would have observed increased mobility at low O_2 environments (*i.e.*, low surface –OH). This was not observed. Thus, our observations are inconsistent with a surface-hydroxide-controlled mechanism, and this could be due to the instability of surface hydroxide at high temperature.[113,114]

We note that both of these mechanisms are able to satisfactorily explain the observed phenomenon of surface migration, but neither is particularly well suited to describing a subsurface diffusion event. Note that Kim *et al.*,[94] and others,[115–117] have highlighted subsurface catalyst diffusion as a potential mechanism for termination of VA-CNT growth, but such subsurface diffusion was not observed in this study at the end of the 10 min catalyst annealing. This disparity suggests there might be a kinetic limitation or temporally-dependent transition wherein Ostwald ripening or subsurface diffusion dominate the catalyst morphology evolution. Moreover, the presence of carbon might influence on these two phenomena in the following VA-CNT growth step, but this remains to be conclusively demonstrated. Uncovering the mechanisms for this process could be critical to achieving sustained CNT chain propagation.[67]

Conclusions

We demonstrated that several hundred ppm of O_2 could accelerate Fe nanoparticle Ostwald ripening, that this effect could be mitigated by high H_2 (as expected if O_2 dominated the process), and that H_2O itself had a minor influence on Fe catalyst nanoparticle evolution. This has important implications for reproducibility in CNT manufacturing, especially with regard to challenging O_2 and moisture control, and VA-CNT macro-scale alignment and density manipulation. For example, creating an O_2-free annealing environment should be favorable for consistent catalyst size modulation in practical CNT manufacturing. Underscoring Oliver *et al.*'s work,[11] this has been realized by replacing gas permeable, plastic (*e.g.*, PTFE) gas delivery tubing with stainless steel tubing to remove O_2 from gas supply lines. Alternatively, a H_2-rich baking step can mitigate residual O_2. Considering the roles of moisture (*i.e.*, no effect on catalyst annealing and a potential benefit to growth at low levels) and the challenge of generating dry reactor conditions (*e.g.*, *via* energy-intensive pumping, time-consuming purging, or specialty, sealed, and automated catalyst delivery systems[66]), intentional water vapor addition to maintain a controlled and stable, low moisture level could be the best route to maintain manufacturing consistency and productivity. Further, taking advantage of O_2 partial pressures in annealing phase, one can precisely manage catalyst nanoparticle size and monodispersity, approaching application-motivated CNT property control. Specifically, high H_2 and low O_2 partial pressure annealing treatment bears the potential to synthesize SWCNT-enriched or narrow chirality distributed CNT arrays for thin film transistors,[118] which has potentially transformative implication for SWCNT manufacturing from earth-abundant, easy-to-manipulate metal catalysts (*e.g.*, Fe). However, for large diameter MWCNTs production, controlling catalyst film thickness[20] might be operationally more straight-forward than tuning O_2 content. Nevertheless, since any atmospheric-pressure annealing condition is beholden to background oxygen and water vapor, controlling O_2 is critical to reduce CNT diameter distributions and limit batch-to-batch hysteresis and variability within continuous growth processes, whether from thick or thin films of catalyst. Lastly, the understanding of gas species effects on Fe-on-Al_2O_3 system not only provides a strategy for catalyst morphology control during CNT

growth, but also should be applicable for other heterogeneous catalysis reactions, informing the fundamental mechanisms at play in the sintering processes that go on in many of the most industrially promising catalytic systems.

Acknowledgements

References

1 S. J. Tans, A. R. M. Verschueren and C. Dekker, *Nature*, 1998, **393**, 49–52.

2 J. Appenzeller, Y. M. Lin, J. Knoch and P. Avouris, *Phys. Rev. Lett.*, 2004, **93**, 196805.

3 A. M. Ionescu and H. Riel, *Nature*, 2011, **479**, 329–337.

4 A. D. Franklin, M. Luisier, S. J. Han, G. Tulevski, C. M. Breslin, L. Gignac, M. S. Lundstrom and W. Haensch, *Nano Lett.*, 2012, **12**, 758–762.

5 M. F. L. De Volder, S. H. Tawfick, R. H. Baughman and A. J. Hart, *Science*, 2013, **339**, 535–539.

6 L. M. Dai, D. W. Chang, J. B. Baek and W. Lu, *Small*, 2012, **8**, 1130–1166.

7 B. Lee, Y. Baek, M. Lee, D. H. Jeong, H. H. Lee, J. Yoon and Y. H. Kim, *Nat. Commun.*, 2015, **6**, 7109.

8 F. Yang, X. Wang, D. Q. Zhang, J. Yang, D. Luo, Z. W. Xu, J. K. Wei, J. Q. Wang, Z. Xu, F. Peng, X. M. Li, R. M. Li, Y. L. Li, M. H. Li, X. D. Bai, F. Ding and Y. Li, *Nature*, 2014, **510**, 522–524.

9 I. Ibrahim, T. Gemming, W. M. Weber, T. Mikolajick, Z. F. Liu and M. H. Rummeli, *ACS Nano*, 2016, **10**, 7248–7266.

10 D. N. Yuan, L. Ding, H. B. Chu, Y. Y. Feng, T. P. McNicholas and J. Liu, *Nano Lett.*, 2008, **8**, 2576–2579.

11 C. R. Oliver, E. S. Polsen, E. R. Meshot, S. Tawfick, S. J. Park, M. Bedewy and A. J. Hart, *ACS Nano*, 2013, **7**, 3565–3580.

12 J. J. Li, M. Bedewy, A. O. White, E. S. Polsen, S. Tawfick and A. J. Hart, *J. Phys. Chem. C*, 2016, **120**, 11277–11287.

13 K. Liu, P. Liu, K. Jiang and S. S. Fan, *Carbon*, 2007, **45**, 2379–2387.

14 K. Hata, D. N. Futaba, K. Mizuno, T. Namai, M. Yumura and S. Iijima, *Science*, 2004, **306**, 1362–1364.

15 G. Y. Zhang, D. Mann, L. Zhang, A. Javey, Y. M. Li, E. Yenilmez, Q. Wang, J. P. McVittie, Y. Nishi, J. Gibbons and H. J. Dai, *Proc. Natl. Acad. Sci. U. S. A.*, 2005, **102**, 16141–16145.

16 A. Magrez, J. W. Seo, R. Smajda, B. Korbely, J. C. Andresen, M. Mionic, S. Casimirius and L. Forro, *ACS Nano*, 2010, **4**, 3702–3708.

17 D. N. Futaba, K. Hata, T. Yamada, K. Mizuno, M. Yumura and S. Iijima, *Phys. Rev. Lett.*, 2005, **95**, 056104.

18 C. L. Pint, S. T. Pheasant, A. N. G. Parra-Vasquez, C. Horton, Y. Q. Xu and R. H. Hauge, *J. Phys. Chem. C*, 2009, **113**, 4125–4133.

19 M. Stadermann, S. P. Sherlock, J. B. In, F. Fornasiero, H. G. Park, A. B. Artyukhin, Y. M. Wang, J. J. De Yoreo, C. P. Grigoropoulos, O. Bakajin, A. A. Chernov and A. Noy, *Nano Lett.*, 2009, **9**, 738–744.

20 K. Hasegawa and S. Noda, *ACS Nano*, 2011, **5**, 975–984.

21 G. D. Nessim, A. Al-Obeidi, H. Grisaru, E. S. Polsen, C. R. Oliver, T. Zimrin, A. J. Hart, D. Aurbach and C. V. Thompson, *Carbon*, 2012, **50**, 4002–4009.

22 D. N. Futaba, K. Hata, T. Namai, T. Yamada, K. Mizuno, Y. Hayamizu, M. Yumura and S. Iijima, *J. Phys. Chem. B*, 2006, **110**, 8035–8038.

23 P. Li and J. Zhang, *J. Mater. Chem.*, 2011, **21**, 11815–11821.

24 W. W. Zhou, S. T. Zhan, L. Ding and J. Liu, *J. Am. Chem. Soc.*, 2012, **134**, 14019–14026.

25 A. R. Harutyunyan, G. G. Chen, T. M. Paronyan, E. M. Pigos, O. A. Kuznetsov, K. Hewaparakrama, S. M. Kim, D. Zakharov, E. A. Stach and G. U. Sumanasekera, *Science*, 2009, **326**, 116–120.

26 C. H. Bartholomew, *Appl. Catal., A*, 2001, **212**, 17–60.

27 F. Tao and P. A. Crozier, *Chem. Rev.*, 2016, **116**, 3487–3539.

28 A. T. Bell, *Science*, 2003, **299**, 1688–1691.

29 K. M. Bratlie, H. Lee, K. Komvopoulos, P. D. Yang and G. A. Somorjai, *Nano Lett.*, 2007, **7**, 3097–3101.

30 R. J. Isaifan, S. Ntais and E. A. Baranova, *Appl. Catal., A*, 2013, **464**, 87–94.

31 S. B. Simonsen, I. Chorkendorff, S. Dahl, M. Skoglundh, J. Sehested and S. Helveg, *J. Am. Chem. Soc.*, 2010, **132**, 7968–7975.

32 S. B. Simonsen, I. Chorkendorff, S. Dahl, M. Skoglundh, J. Sehested and S. Helveg, *J. Catal.*, 2011, **281**, 147–155.

33 A. D. Benavidez, L. Kovarik, A. Genc, N. Agrawal, E. M. Larsson, T. W. Hansen, A. M. Karim and A. K. Datye, *ACS Catal.*, 2012, **2**, 2349–2356.

34 N. Chaabane, R. Lazzari, J. Jupille, G. Renaud and E. A. Soares, *J. Phys. Chem. C*, 2012, **116**, 23362–23370.

35   S. B. Simonsen, I. Chorkendorff, S. Dahl, M. Skoglundh, K. Meinander, T. N. Jensen, J. V. Lauritsen and S. Helveg, *J. Phys. Chem. C*, 2012, **116**, 5646–5653.

36   F. Behafarid, S. Pandey, R. E. Diaz, E. A. Stach and B. R. Cuenya, *Phys. Chem. Chem. Phys.*, 2014, **16**, 18176–18184.

37   S. Bonanni, K. Ait-Mansour, W. Harbich and H. Brune, *J. Am. Chem. Soc.*, 2014, **136**, 8702–8707.

38   G. Hofmann, A. Rochet, E. Ogel, M. Casapu, S. Ritter, M. Ogurreck and J. D. Grunwaldt, *RSC Adv.*, 2015, **5**, 6893–6905.

39   P. T. Z. Adibi, T. Pingel, E. Olsson, H. Gronbeck and C. Langhammer, *ACS Nano*, 2016, **10**, 5063–5069.

40   S. Y. Zhang, M. Cargnello, W. Cai, C. B. Murray, G. W. Graham and X. Q. Pan, *J. Catal.*, 2016, **337**, 240–247.

41   P. T. Z. Adibi, F. Mazzotta, T. J. Antosiewicz, M. Skogundh, H. Gronbeck and C. Langharnmer, *ACS Catal.*, 2015, **5**, 426–432.

42   R. J. Liu, P. A. Crozier, C. M. Smith, D. A. Hucul, J. Blackson and G. Salaita, *Microsc. Microanal.*, 2004, **10**, 77–85.

43   R. J. Liu, P. A. Crozier, C. M. Smith, D. A. Hucul, J. Blackson and G. Salaita, *Appl. Catal., A*, 2005, **282**, 111–121.

44   S. B. Simonsen, I. Chorkendorff, S. Dahl, M. Skoglundh and S. Helveg, *Surf. Sci.*, 2016, **648**, 278–283.

45   F. Yang, M. S. Chen and D. W. Goodman, *J. Phys. Chem. C*, 2009, **113**, 254–260.

46   K. J. Hu, S. R. Plant, P. R. Ellis, C. M. Brown, P. T. Bishop and R. E. Palmer, *J. Am. Chem. Soc.*, 2015, **137**, 15161–15168.

47   T. E. Martin, P. L. Gai and E. D. Boyes, *ChemCatChem*, 2015, **7**, 3705–3711.

48   R. van den Berg, T. E. Parmentier, C. F. Elkjaer, C. J. Gommes, J. Sehested, S. Helveg, P. E. de Jongh and K. P. de Jong, *ACS Catal.*, 2015, **5**, 4439–4448.

49   D. Kistamurthy, A. M. Saib, D. J. Moodley, J. W. Niemantsverdriet and C. J. Weststrate, *J. Catal.*, 2015, **328**, 123–129.

50   F. LeNormand, A. Borgna, T. F. Garetto, C. R. Apesteguia and B. Moraweck, *J. Phys. Chem.*, 1996, **100**, 9068–9076.

51   H. Hirata, K. Kishita, Y. Nagai, K. Dohmae, H. Shinjoh and S. Matsumoto, *Catal. Today*, 2011, **164**, 467–473.

52   M. H. Zhu and I. E. Wachs, *ACS Catal.*, 2016, **6**, 722–732.

53   S. Z. Li, S. Krishnamoorthy, A. W. Li, G. D. Meitzner and E. Iglesia, *J. Catal.*, 2002, **206**, 202–217.

54   M. Lefevre, E. Proietti, F. Jaouen and J. P. Dodelet, *Science*, 2009, **324**, 71–74.

55   X. G. Guo, G. Z. Fang, G. Li, H. Ma, H. J. Fan, L. Yu, C. Ma, X. Wu, D. H. Deng, M. M. Wei, D. L. Tan, R. Si, S. Zhang, J. Q. Li, L. T. Sun, Z. C. Tang, X. L. Pan and X. H. Bao, *Science*, 2014, **344**, 616–619.

56   V. Jourdain and C. Bichara, *Carbon*, 2013, **58**, 2–39.

57   Y. Li, R. L. Cui, L. Ding, Y. Liu, W. W. Zhou, Y. Zhang, Z. Jin, F. Peng and J. Liu, *Adv. Mater.*, 2010, **22**, 1508–1515.

58   P. B. Amama, C. L. Pint, L. McJilton, S. M. Kim, E. A. Stach, P. T. Murray, R. H. Hauge and B. Maruyama, *Nano Lett.*, 2009, **9**, 44–49.

59   R. M. Wyss, J. E. Klare, H. G. Park, A. Noy, O. Bakajin and V. Lulevich, *ACS Appl. Mater. Interfaces*, 2014, **6**, 21019–21025.

60   K. L. Jiang, J. P. Wang, Q. Q. Li, L. A. Liu, C. H. Liu and S. S. Fan, *Adv. Mater.*, 2011, **23**, 1154–1161.

61   X. M. Sun, T. Chen, Z. B. Yang and H. S. Peng, *Acc. Chem. Res.*, 2013, **46**, 539–549.

62   M. Bedewy, B. Viswanath, E. R. Meshot, D. N. Zakharov, E. A. Stach and A. J. Hart, *Chem. Mater.*, 2016, **28**, 3804–3813.

63   A. J. Hart and A. H. Slocum, *J. Phys. Chem. B*, 2006, **110**, 8250–8257.

64   S. Hofmann, R. Blume, C. T. Wirth, M. Cantoro, R. Sharma, C. Ducati, M. Havecker, S. Zafeiratos, P. Schnoerch, A. Oestereich, D. Teschner, M. Albrecht, A. Knop-Gericke, R. Schlogl and J. Robertson, *J. Phys. Chem. C*, 2009, **113**, 1648–1656.

65   E. R. Meshot, E. Verploegen, M. Bedewy, S. Tawfick, A. R. Woll, K. S. Green, M. Hromalik, L. J. Koerner, H. T. Philipp, M. W. Tate, S. M. Gruner and A. J. Hart, *ACS Nano*, 2012, **6**, 5091–5101.

66   C. R. Oliver, W. Westrick, J. Koehler, A. Brieland-Shoultz, I. Anagnostopoulos-Politis, T. Cruz-Gonzalez and A. J. Hart, *Rev. Sci. Instrum.*, 2013, **84**, 115105.

67   D. L. Plata, E. R. Meshot, C. M. Reddy, A. J. Hart and P. M. Gschwend, *ACS Nano*, 2010, **4**, 7185–7192.

68   E. Teblum, Y. Gofer, C. L. Pint and G. D. Nessim, *J. Phys. Chem. C*, 2012, **116**, 24522–24528.

69   M. Xu, D. N. Futaba, M. Yumura and K. Hata, *ACS Nano*, 2012, **6**, 5837–5844.

70   S. S. Fan, M. G. Chapline, N. R. Franklin, T. W. Tombler, A. M. Cassell and H. J. Dai, *Science*, 1999, **283**, 512–514.

71   M. Bedewy and A. J. Hart, *Nanoscale*, 2013, **5**, 2928–2937.

72   J. H. Han, R. A. Graff, B. Welch, C. P. Marsh, R. Franks and M. S. Strano, *ACS Nano*, 2008, **2**, 53–60.

73   D. L. Plata, A. J. Hart, C. M. Reddy and P. M. Gschwend, *Environ. Sci. Technol.*, 2009, **43**, 8367–8373.

74   A. Shaikjee and N. J. Coville, *Carbon*, 2012, **50**, 1099–1108.

75   M. H. Rummeli, E. Borowiak-Palen, T. Gemming, T. Pichler, M. Knupfer, M. Kalbac, L. Dunsch, O. Jost, S. R. P. Silva, W. Pompe and B. Buchner, *Nano Lett.*, 2005, **5**, 1209–1215.

76   Q. Wen, W. Z. Qian, F. Wei and G. Q. Ning, *Nanotechnology*, 2007, **18**, 215610.

77   C. L. Cheung, A. Kurtz, H. Park and C. M. Lieber, *J. Phys. Chem. B*, 2002, **106**, 2429–2433.

78   Y. B. Chen and J. Zhang, *Carbon*, 2011, **49**, 3316–3324.

79   M. F. C. Fiawoo, A. M. Bonnot, H. Amara, C. Bichara, J. Thibault-Penisson and A. Loiseau, *Phys. Rev. Lett.*, 2012, **108**, 195503.

80   P. Li, X. Zhang and J. Liu, *Chem. Mater.*, 2016, **28**, 870–875.

81 S. M. Bachilo, L. Balzano, J. E. Herrera, F. Pompeo, D. E. Resasco and R. B. Weisman, *J. Am. Chem. Soc.*, 2003, **125**, 11186–11187.

82 W. E. Alvarez, F. Pompeo, J. E. Herrera, L. Balzano and D. E. Resasco, *Chem. Mater.*, 2002, **14**, 1853–1858.

83 D. E. Resasco, W. E. Alvarez, F. Pompeo, L. Balzano, J. E. Herrera, B. Kitiyanan and A. Borgna, *J. Nanopart. Res.*, 2002, **4**, 131–136.

84 C. Journet, W. K. Maser, P. Bernier, A. Loiseau, M. L. delaChapelle, S. Lefrant, P. Deniard, R. Lee and J. E. Fischer, *Nature*, 1997, **388**, 756–758.

85 R. J. Klee and T. E. Graedel, *Annu. Rev. Environ. Resour.*, 2004, **29**, 69–107.

86 G. D. Nessim, A. J. Hart, J. S. Kim, D. Acquaviva, J. H. Oh, C. D. Morgan, M. Seita, J. S. Leib and C. V. Thompson, *Nano Lett.*, 2008, **8**, 3587–3593.

87 M. Cantoro, S. Hofmann, S. Pisana, V. Scardaci, A. Parvez, C. Ducati, A. C. Ferrari, A. M. Blackburn, K. Y. Wang and J. Robertson, *Nano Lett.*, 2006, **6**, 1107–1112.

88 E. W. Wong, M. J. Bronikowski, M. E. Hoenk, R. S. Kowalczyk and B. D. Hunt, *Chem. Mater.*, 2005, **17**, 237–241.

89 J. B. In, C. P. Grigoropoulos, A. A. Chernov and A. Noy, *ACS Nano*, 2011, **5**, 9602–9610.

90 Y. Hu, L. X. Kang, Q. C. Zhao, H. Zhong, S. C. Zhang, L. W. Yang, Z. Q. Wang, J. J. Lin, Q. W. Li, Z. Y. Zhang, L. M. Peng, Z. F. Liu and J. Zhang, *Nat. Commun.*, 2015, **6**, 6099.

91 S. Sakurai, M. Inaguma, D. N. Futaba, M. Yumura and K. Hata, *Small*, 2013, **9**, 3584–3592.

92 G. S. Parkinson, Z. Novotny, G. Argentero, M. Schmid, J. Pavelec, R. Kosak, P. Blaha and U. Diebold, *Nat. Mater.*, 2013, **12**, 724–728.

93 S. Sakurai, H. Nishino, D. N. Futaba, S. Yasuda, T. Yamada, A. Maigne, Y. Matsuo, E. Nakamura, M. Yumura and K. Hata, *J. Am. Chem. Soc.*, 2012, **134**, 2148–2153.

94 S. M. Kim, C. L. Pint, P. B. Amama, D. N. Zakharov, R. H. Hauge, B. Maruyama and E. A. Stach, *J. Phys. Chem. Lett.*, 2010, **1**, 918–922.

95 P. B. Amama, C. L. Pint, S. M. Kim, L. McJilton, K. G. Eyink, E. A. Stach, R. H. Hauge and B. Maruyama, *ACS Nano*, 2010, **4**, 895–904.

96 J. W. Yang, S. Esconjauregui, R. Xie, H. Sugime, T. Makaryan, L. D'Arsie, D. L. G. Arellano, S. Bhardwaj, C. Cepek and J. Robertson, *J. Phys. Chem. C*, 2014, **118**, 18683–18692.

97 G. F. Zhong, J. W. Yang, H. Sugime, R. Rao, J. W. Zhao, D. M. Liu, A. Harutyunyan and J. Robertson, *Carbon*, 2016, **98**, 624–632.

98 G. F. Zhong, J. H. Warner, M. Fouquet, A. W. Robertson, B. A. Chen and J. Robertson, *ACS Nano*, 2012, **6**, 2893–2903.

99 S. Pisana, M. Cantoro, A. Parvez, S. Hofmann, A. C. Ferrari and J. Robertson, *Physica E*, 2007, **37**, 1–5.

100 R. H. Ouyang, J. X. Liu and W. X. Li, *J. Am. Chem. Soc.*, 2013, **135**, 1760–1771.

101 A. Magrez, R. Smajda, J. W. Seo, E. Horvath, P. R. Ribic, J. C. Andresen, D. Acquaviva, A. Olariu, G. Laurenczy and L. Forro, *ACS Nano*, 2011, **5**, 3428–3437.

102 S. Hofmann, *Auger- and X-ray Photoelectron Spectroscopy in Materials Science: A User-Oriented Guide*, Springer, Germany, 2013.

103 S. A. Steiner, T. F. Baumann, B. C. Bayer, R. Blume, M. A. Worsley, W. J. MoberlyChan, E. L. Shaw, R. Schlogl, A. J. Hart, S. Hofmann and B. L. Wardle, *J. Am. Chem. Soc.*, 2009, **131**, 12144–12154.

104 X. F. Lai, T. P. St Clair and D. W. Goodman, *Faraday Discuss.*, 1999, **114**, 279–284.

105 M. Abbasi, J. Lee, M. Shin, Y. Kim and Y. Kang, *Appl. Surf. Sci.*, 2014, **313**, 116–122.

106 C. Zhang, F. Yan, C. S. Allen, B. C. Bayer, S. Hofmann, B. J. Hickey, D. Cott, G. Zhong and J. Robertson, *J. Appl. Phys.*, 2010, **108**, 024311.

107 B. C. Bayer, C. Zhang, R. Blume, F. Yan, M. Fouquet, C. T. Wirth, R. S. Weatherup, L. Lin, C. Baehtz, R. A. Oliver, A. Knop-Gericke, R. Schlogl, S. Hofmann and J. Robertson, *J. Appl. Phys.*, 2011, **109**, 114314.

108 A. P. Markusse, B. F. M. Kuster, D. C. Koningsberger and G. B. Marin, *Catal. Lett.*, 1998, **55**, 141–145.

109 L. R. Merte, M. Ahmadi, F. Behafarid, L. K. Ono, E. Lira, J. Matos, L. Li, J. C. Yang and B. R. Cuenya, *ACS Catal.*, 2013, **3**, 1460–1468.

110 A. Kolmakov and D. W. Goodman, *Catal. Lett.*, 2000, **70**, 93–97.

111 S. Porsgaard, L. R. Merte, L. K. Ono, F. Behafarid, J. Matos, S. Helveg, M. Salmeron, B. R. Cuenya and F. Besenbacher, *ACS Nano*, 2012, **6**, 10743–10749.

112 D. Cappus, C. Xu, D. Ehrlich, B. Dillmann, C. A. Ventrice, K. Alshamery, H. Kuhlenbeck and H. J. Freund, *Chem. Phys.*, 1993, **177**, 533–546.

113 V. Cimalla, M. Baeumler, L. Kirste, M. Prescher, B. Christian, T. Passow, F. Benkhelifa, F. Bernhardt, G. Eichapfel, M. Himmerlich, S. Krischok and J. Pezoldt, *Mater. Sci. Appl.*, 2014, **5**, 628–638.

114 G. Krautheim, T. Hecht, S. Jakschik, U. Schroder and W. Zahn, *Appl. Surf. Sci.*, 2005, **252**, 200–204.

115 W. D. Cho, M. Schulz and V. Shanov, *Carbon*, 2014, **69**, 609–620.

116 Z. L. Gao, X. F. Zhang, K. Zhang and M. M. F. Yuen, *J. Phys. Chem. C*, 2015, **119**, 15636–15642.

117 S. Jeong, J. Lee, H. C. Kim, J. Y. Hwang, B. C. Ku, D. N. Zakharov, B. Maruyama, E. A. Stach and S. M. Kim, *Nanoscale*, 2016, **8**, 2055–2062.

118 S. J. Kang, C. Kocabas, T. Ozel, M. Shim, N. Pimparkar, M. A. Alam, S. V. Rotkin and J. A. Rogers, *Nat. Nanotechnol.*, 2007, **2**, 230–236.